Journal of Materials Chemistry A

PAPER

View Article Online
View Journal | View Issue

Cite this: J. Mater. Chem. A, 2018, 6, 11985

Effect of donor length on electronic structures and charge transport polarity for DTDPP-based D–A copolymers: a computational study based on a super-exchange model†

Feifei He,‡[a] Changli Cheng,‡[a] Hua Geng,[b]* Yuanping Yi[c] and Zhigang Shuai[a]*

Received 8th March 2018
Accepted 17th May 2018

DOI: 10.1039/c8ta02175a

rsc.li/materials-a

With the number of thiophene units increasing from 1 to 5 for dithiophenyldiketopyrrolopyrrole-(*n*-thiophene) (DTDPP-*n*T) polymers, we found that their band gap increases and their bandwidth narrows from first-principles computations; their transport polarity changes from n-type (n = 1, 2, 3) to ambipolar (n = 4) and finally to p-type (n = 5). The electronic structures and transport polarity can be understood from an intra-chain super-exchange (SE) mechanism. For different donor lengths, the SE model changed from sandwich-type (n = 1–4) to staggered-type (n = 5). As for n = 1–4, the charge transport polarity is determined with the relative magnitude of polarized LUMO and HOMO energy differences of the fragment (DTDPP/*n*T). In contrast, DTDPP-5T reveals p-type transport polarity due to the staggered-type SE mechanism. In addition, inter-chain coupling and band edge shift also contribute to the conversion of transport polarity.

1. Introduction

Conjugated polymers play an important role in applications of optoelectronic devices such as organic photovoltaics (OPVs)[1–6] and organic field effect transistors (OFETs)[7–12] because of their easy-to-modify structure, solution processability and low device fabrication cost. Donor–acceptor (D–A) copolymers, which contain electron-donating (D) and electron-withdrawing (A) repeating units, have promoted the rapid development of OFETs.[13] D–A copolymers usually have great potential in obtaining high mobility[14–17] and generally show three types of transport characteristics, *i.e.*, p-type (hole transport property),[14,18–20] n-type (electron transport property)[21–24] and ambipolar transport property.[25–27]

Although the charge transport performance and polarity of D–A copolymers are influenced and restricted by many factors, such as the side chain, molecular weight, solubility, microstructure, charge injection and inter-chain or intra-chain charge transport,[28,29] scientists have designed and synthesized highly oriented polymers to understand their intrinsic charge transport properties.[30–35] Alan Heeger *et al.* demonstrated that the charge mainly delocalized on the backbone of polymer nanowires; they suggested that intra-chain charge transport makes a dominant contribution; there is occasionally inter-chain charge hopping, and then the ultra-small intra-chain effective mass promises high carrier mobility.[31] In order to achieve a small effective mass, some strategies, such as alloying in inorganic semiconductors[36–38] and blending in organic small molecule semiconductors,[39] have been suggested. To understand the charge transport mechanism, we first extended SE models, which have so far been mostly applied in biochemical simulations,[40] to organic solids recently,[41,42] and then we further applied an SE model in complex D–A copolymers, and it can be suggested that the long-range SE mechanism is an effective way to achieve a small effective mass and thus high mobility.[43]

Among D–A polymers, diketopyrrolopyrrole (DPP)-based copolymers have been widely studied and exhibit diversified transport polarity.[17–19,25–27] Their ambipolar property makes them special, since single-component ambipolar materials would be of interest for complementary-like logic circuits[44–46] and light-emitting field-effect transistor applications.[47,48] To obtain different polarity materials, scientists have tried a variety of methods to chemically modify DPP-based copolymers. One strategy features replacement of flanked thiophenes with different electron withdrawing moieties including thiazoles, pyridines, *etc.*[49–51] In another route, attempts have been made to synthesize different D–A copolymers with DPP using varieties of

[a]MOE Key Laboratory of Organic OptoElectronics and Molecular Engineering, Department of Chemistry, Tsinghua University, Beijing 100084, China. E-mail: zgshuai@tsinghua.edu.cn

[b]Department of Chemistry, Capital Normal University, Beijing 100048, China. E-mail: hgeng@cnu.edu.cn

[c]Beijing National Laboratory for Molecular Sciences, CAS Key Laboratory of Organic Solids, Institute of Chemistry, Chinese Academy of Sciences, Beijing 100190, China

† Electronic supplementary information (ESI) available. See DOI: 10.1039/c8ta02175a

‡ Feifei He and Changli Cheng contributed equally to this paper.

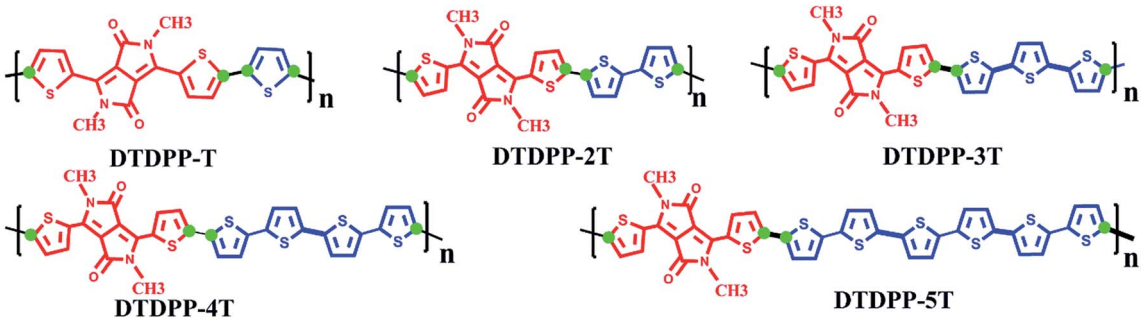

Scheme 1 Investigated systems for DTDPP-*n*T (n = 1–5). The linkage sites in both donors and acceptors are marked by circles.

donor fragments. Copolymers containing DTDPP show transport polarity changing from electron transport to ambipolar and finally to hole transport, when combined with different lengths of donors.[18,19,21,27] Similarly, changing the number and sequence of units in the polymer will affect the properties of the polymer, and the study of repeating units will provide a basis for the extrapolation of polymer properties.[52–54] For example, Hogan *et al.* analysed the trends in the electronic levels with the oligomer length, and then obtained the band gap after correcting the long-range behaviour;[52] to expand the diversity of candidate compounds for organic polymer photovoltaics, the Hutchison group utilized a strong "sequence effect" to obtain tetramer units with HOMO–LUMO gap changes of ~0.2 eV.[53]

In this paper, combining electronic structures, intra-chain SE, effective mass, and inter-chain coupling calculations, we investigated the dependence of charge transport on the length of donor segments for (DTDPP-*n*T) polymers (Scheme 1). Here, we put forward a novel SE model dependent relative energy alignment of donor/acceptor fragments. We found that there exists a continuous change from n-type to ambipolar and finally to p-type with the donor length increasing. Based on the SE model for complex D–A copolymers, we provide molecular insight into the charge transport polarity in D–A copolymers.

2. Computational details and model

With the progress in material processing techniques, polymer nanowires and highly crystalline thin films have been prepared, and remarkably high mobility has been demonstrated.[31] Therefore, the D–A copolymer backbone can be regarded as a one-dimensional periodic structure approximately. Side-chains were replaced by methyl to simplify calculations. The energy levels of donors, acceptors and (D–A)*n* (n = 1–4) oligomers are calculated at the B3LYP/6-31G(d) level with the GAUSSIAN09 code.[55] The geometric structure of the 1D periodic polymer chain was optimized at the B3LYP/6-31G(d) level with the CRYSTAL14 code.[56] A uniform 21 × 1 × 1 Monkhorst–Pack *k*-point mesh was employed for all D–A copolymers. We calculated 41 *k*-points between the gamma point (centre of the Brillouin zone, BZ) and the edge of the first BZ to obtain the band structures. The effective mass for one-dimensional crystals is obtained from the second order derivative of the band energy. The ultra-small effective mass had been demonstrated from long-range intra-chain SE coupling.[43] Based on the Larsson partition approach, both site energy correction and each individual molecular orbital of the bridge contribution can be accounted for.[41]

To understand the properties of infinitely long D–A copolymers through small molecular blocks, the donor and acceptor linked by covalent bonds must have relatively localized molecular orbital characteristics, and then the supramolecular orbitals are the linear combination of monomer orbitals. Taking the DTDPP-2T system as an example (see Fig. S1 (a) in the ESI†), the most relevant orbitals of charge transfer (LUMO+1, LUMO, HOMO and HOMO−1) of ADA can only be regarded as the combinations of the molecular orbitals of DTDPP with 2T, not as DPP with 4T. Such a partition is also supported by the band structure analysis as shown in Fig. S1(b).†

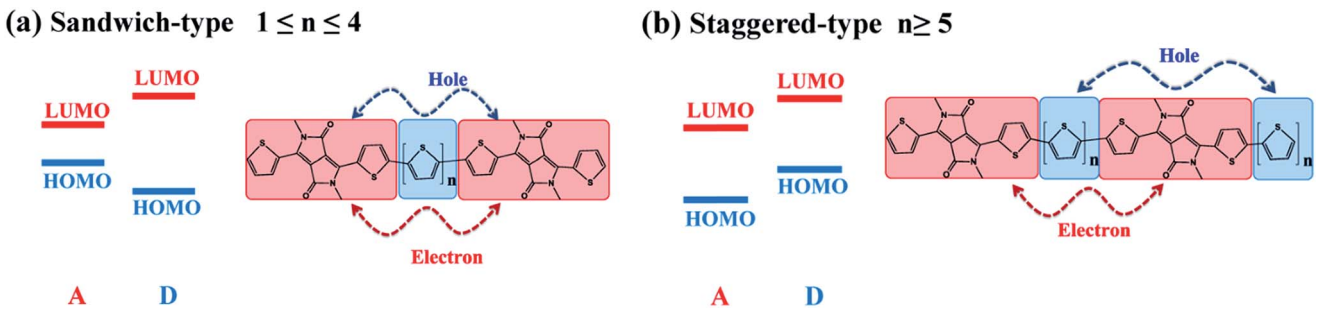

Scheme 2 SE coupling model and the corresponding energy alignment.

The polarization corrected energies of the HOMO and LUMO for acceptor segments are all lower than those of donor segments; the energy alignment presents staggered-type, and we named it the staggered-type SE model. When acceptors have a narrow HOMO–LUMO gap, the LUMO of the acceptor moiety is lower than that of the donor, while the HOMO of the acceptor is higher than that of the donor. The energy alignment reveals a sandwich-type character, and we named it the sandwich-type SE model. And therefore, we put forward two kinds of SE models named staggered-type and sandwich-type according to the relative polarized energy alignment between the donor and the acceptor fragment, as shown in Scheme 2.

According to the energy alignment of polarized donor and acceptor segments, the SE model can be chosen as mentioned above. With the length of the donor increasing, the SE coupling model changed from sandwich-type to staggered-type, since the relative energy alignment varies significantly for DTDPP and *n*T segments. For staggered-type, the triad system is DTDPP-5T-DTDPP (5T-DTDPP-5T) for electrons (holes). However, with respect to the sandwich-type model, the triad system is both DTDPP-*n*T-DTDPP for electrons and holes. The Hamiltonian and the overlap matrix of the triad system can be projected to the fragment molecular orbitals as follows:

$$H = \begin{pmatrix} \varepsilon_1 & V_{12} & V_{1B} \\ V_{21} & \varepsilon_2 & V_{2B} \\ V_{B1} & V_{B2} & \varepsilon_B \end{pmatrix} \quad (1)$$

$$S = \begin{pmatrix} 1 & S_{12} & S_{1B} \\ S_{21} & 1 & S_{2B} \\ S_{B1} & S_{B2} & 1 \end{pmatrix} \quad (2)$$

here, the matrix element $\varepsilon_i = \langle\psi_i|H|\psi_i\rangle$, $V_{ij} = V_{ji} = \langle\psi_i|H|\psi_j\rangle$ and $S_{ij} = S_{ji} = \langle\psi_i|\psi_j\rangle$. The fragment molecular orbital $\psi_{i/j}$ as a basis set was normalized without hydrogen; this denotes that the oligomeric triad orbitals are localized on donor or acceptor moieties. For hole (electron) transport, ψ_1 and ψ_2 are the HOMO (LUMO) of D1 (A1) and D2 (A2), respectively, and ψ_B represents the molecular orbitals of the bridge A (D) fragment. By means of Löwdin's symmetric transformation, the site energy corrected from polarization can be considered as follows:[43]

$$\tilde{H} = S^{-1/2}HS^{-1/2} = \begin{pmatrix} \tilde{\varepsilon}_1 & \tilde{V}_{12} & \tilde{V}_{1B} \\ \tilde{V}_{21} & \tilde{\varepsilon}_2 & \tilde{V}_{2B} \\ \tilde{V}_{B1} & \tilde{V}_{B2} & \tilde{\varepsilon}_B \end{pmatrix} \quad (3)$$

Next, using the Larsson partition technique in connection with the perturbation scheme, we obtain effective electronic coupling:

$$V^{\text{eff}} = V^{\text{im}} + \sum_{b\in B} \frac{\tilde{V}_{1b}\tilde{V}_{b2}}{E - \tilde{\varepsilon}_b} \quad (4)$$

The implicit ter.m is the Hamiltonian matrix element (V_{12}) obtained through Hamiltonian projection of the triad system on the orthogonalized fragment basis and substantially weaker than its explicit counterpart. $\tilde{V}_{1b}$ and $\tilde{V}_{b2}$ denote coupling of the bridge orbital (b) with the frontier orbitals of the two adjacent fragments (1 and 2); E and $\tilde{\varepsilon}_b$ correspond to the energies of the adiabatic and bridge levels in the triad oligomer, respectively.

3. Results and discussion

3.1 Geometric and electronic structures

The static disorders in D–A copolymers, such as relative orientation and torsional rotation between donors and acceptors, are beyond the scope of this work and not considered here. According to one-dimensional periodic structure optimization, we found that the DA units show good planarity and little bond length change. The band structures of DTDPP-*n*T ($n = 1, 4, 5$) are shown in Fig. 1. When the donor length increases, the band dispersion becomes smaller and smaller with the increased band gap. From DTDPP-T to DTDPP-5T, the valence bandwidth (VBW) decreased from 579 to 175 meV, while the conduction bandwidth (CBW) changed from 675 to 119 meV, respectively. The VBW and CBW turn narrower and narrower with the number of thiophene units increasing. The CBW decreases more drastically than the VBW; the CBW and VBW are close for DTDPP-4T, while the CBW is smaller than the VBW for DTDPP-5T. Thus, the ratio of VBW and CBW is 0.78, 1.06 and 1.47, respectively. The relative magnitude of the VBW and CBW suggests charge transport polarity variation. The more delocalized the charge density distributions are, the larger the bandwidth will be. On comparing the charge density distribution for different donor lengths, more and more localized charge densities have been found. As can be seen from Fig. 1, the partial charge density at the high symmetry points of the valence band (VB) and conduction band (CB) of DTDPP-T, DTDPP-4T and DTDPP-5T is qualitatively consistent with the bandwidth changes.

It is interesting that the band gap monotonically increases with the number of thiophene units; the detailed calculation results obtained by the first principles and extrapolation method can be seen in Fig. S2.† The band gap changes by about 284 meV from 1337 to 1621 meV. The main component of the VB and CB from DTDPP segment contribution, and the addition of the thiophene moiety make the original band dispersion turn smaller (Fig. 1). In the sandwich-type SE model, a larger band gap originates from the reduction of the bandwidth for the valence and the conduction band. Therefore, the band gap of the entire copolymer is approximately determined from the HOMO–LUMO gap of the isolated DTDPP unit and the hole and electron SE coupling (Fig. 2). The stronger the SE coupling is, the bigger the dispersion and the narrower the band gap. Thus, band gap tuning in D–A organic semiconductors can be realized through control of the donor length under specified conditions.

With the band gap decreasing with the increase of donor length, the bottom of the conduction band and the top of the valence band both shift upward. According to the extrapolation method (Fig. S2 in the ESI†), there is a continuous change of the HOMO (−4.756 to −4.676 eV) and LUMO (−3.419 to −3.055 eV) from DTDPP-T to DTDPP-5T. The HOMO energy level shifts upward by about 0.08 eV, and the LUMO level shifts upward by 0.36 eV. In the fabrication of OFETs, organic polymers are often spin-coated on electrodes, to a certain extent, causing the electrode work function to drop accordingly. Taking Au as an

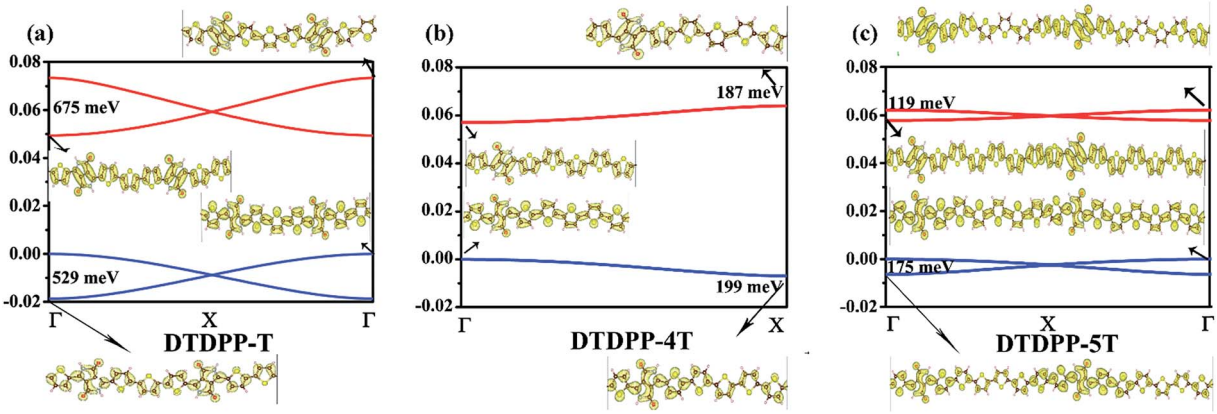

Fig. 1 Band structures and partial charge densities at high symmetry points for DTDPP-nT (n = 1, 4, 5).

example, its work function of 5.24 drops to 4.19 eV, when copolymers are spin-coated on it. In this paper, we regard the Au work function as 4.2 eV, which is in the middle of the band gap of polymers. The upward shift of the LUMO energy level enlarges the injection barrier of electron transfer, while the increasing HOMO energy level decreases the injection barrier of hole transfer.

To understand the modulation of the bandwidth from molecular insight into the polymer backbone, we recall one-dimensional band structures in a tight-binding model:

$$W = \begin{cases} 4V \\ \sqrt{(\Delta\varepsilon/2)^2 + 4V^2} - \Delta\varepsilon/2 = \begin{cases} 2V & \Delta\varepsilon = 0 \\ 4V^{\text{eff}} & 0 < \Delta\varepsilon \ll V \\ & \Delta\varepsilon \gg V \end{cases} \end{cases} \quad (5)$$

$$m^* = \frac{\hbar^2}{a^2V^2}\left[(\Delta\varepsilon/2)^2 + 4V^2\right]^{1/2} = \begin{cases} \dfrac{\hbar^2}{2(a/2)^2V} & \Delta\varepsilon \ll V \\ \dfrac{\hbar^2}{2a^2V^{\text{eff}}} & \Delta\varepsilon \gg V \end{cases} \quad (6)$$

here, V is the nearest neighbour direct coupling between two units, $\Delta\varepsilon$ is the site energy difference, and a is the length of the unit cell. In D–A copolymers ($\Delta\varepsilon \gg V$), $V^{\text{eff}} = V^2/\Delta\varepsilon$ is the bond-mediated SE coupling, and the effective mass is defined by the SE coupling (V^{eff}) and the length of the unit cell. In homopolymer systems ($\Delta\varepsilon \ll V$), the effective mass is determined by direct coupling (V).

It is interesting that there exists a good linear relationship between bandwidths and SE couplings as shown in Fig. 2. The larger the SE coupling is, the wider the bandwidth is. With the length of the donor increasing, the CBW drops faster than the VBW. Here DTDPP-5T is an exception, since the staggered-type model is applied instead and will be explained in the next section. Although the bandwidths of homopolymers ($4V$) are much larger than those of D–A copolymers ($4V^{\text{eff}}$), the long-range SE mechanism provides an ultra-small effective mass and high performance charge transport for D–A copolymers.

3.2 The intra-chain charge transfer

Inspired by the SE mechanism in D–A copolymers, we focus on intra-chain charge transport parameters: intra-chain SE coupling and effective mass. As shown in Scheme 1, five copolymers have been investigated from DTDPP-T to DTDPP-5T. Based on the polarized energy alignment between donors and acceptors, as seen in Fig. 3(A) and Scheme 2, the HOMO–LUMO gap becomes narrower and narrower with the donor length increasing. Compared with isolated DTDPP and nT moieties, the polarization effect has a large impact on the relative molecular orbital energy difference of the fragment. The HOMO of nT (n = 1–4) is lower than that of DTDPP, and the LUMO of nT (n = 1–4) is higher than that of DTDPP. The relative energy alignment between nT (n = 1–4) and DTDPP reveals

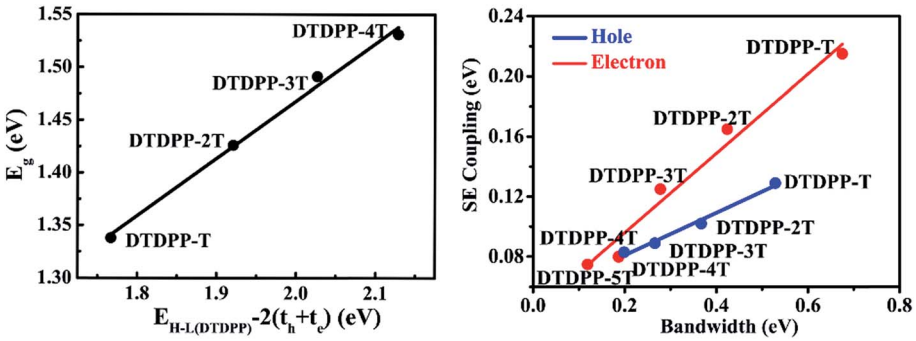

Fig. 2 The dependence of band gaps and bandwidths on SE couplings.

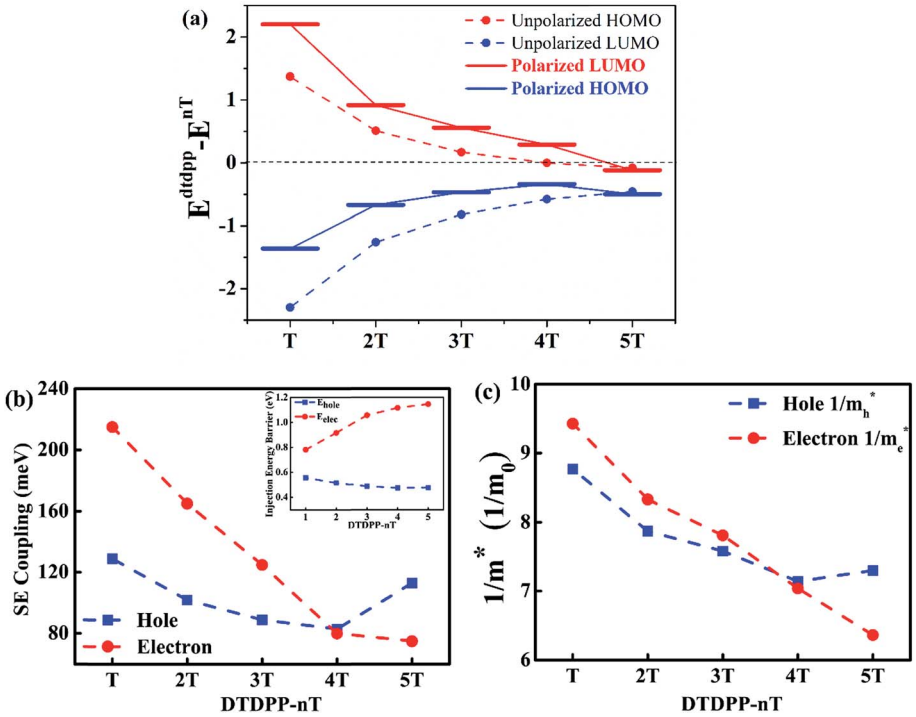

Fig. 3 (a) Unpolarized and polarized molecular orbital energy difference between DTDPP and *n*T; (b) dependence of intra-chain SE coupling on the donor length for electrons and holes (inset of (b): injection barrier for electrons and holes); (c) dependence of the inverse of the effective mass on the donor length for electrons and holes.

a sandwich-type character. In contrast, 5T reveals a higher HOMO than DTDPP, while the LUMO of 5T is still higher than that of DTDPP; DTDPP-5T presents a staggered-type energy alignment between 5T and DTDPP. Therefore, we adopt the sandwich-type SE model for DTDPP-*n*T (n = 1–4), while the staggered-type model is applied for DTDPP-*n*T (n = 5) instead; the corresponding SE coupling of holes and electrons is calculated from the Larsson-partition method, and the effective mass is evaluated from the second order derivative of band energy, as shown in Fig. 3.

As can be seen from Fig. 3(b), the hole SE coupling decreases gradually and increases when the donor length increases up to 5T, but the electron SE coupling dropped drastically with the donor length increasing. For short chain, the electron SE coupling is larger than the hole, and as the chain length increases, the two become close each other and finally the hole SE coupling dominates. Compared with the highest ever reported hole mobility for CDT-PT,[31] it should be noted that DTDPP-T reveals a comparable ultra-small effective mass for electrons. At the same time, balance electron and hole effective masses ($1.140/0.142m_0$) are found for DTDPP-4T. The reciprocal of the effective mass presents a similar tendency as SE coupling, which suggests that the ultra-small effective mass originates from the long range SE mechanism. Both the SE coupling and reciprocal of the effective mass indicate that transfer polarity changes from n-type to ambipolar and to p-type finally.

In addition, accompanied with the increasing donor length, the hole injection barrier reveals a minor reduction from 0.63 to 0.47 eV, However, the electron injection barrier increases significantly from 0.56 to 1.17 eV. Charge injection favours hole transport and adversely affects electron transport and also contributes to transport polarity change. To understand the variation of charge transport polarity from molecular insight, we employed the tight binding Hückel approximation to express the second term of eqn (4) explicitly as follows:

$$V^{\mathrm{eff}}_{\mathrm{hole/elec}} \propto C^{\mathrm{D1(A1)}} C^{\mathrm{Dn(An)}} \cos(\phi_{\mathrm{DA}}) \cos(\phi_{\mathrm{AD}}) \sum_{v \in \mathrm{A(D)}} \frac{C_v^{\mathrm{A1(D1)}} C_v^{\mathrm{An(Dn)}}}{E - \varepsilon_v^{\mathrm{A(D)}}} \quad (7)$$

C is the molecular orbital coefficient. D_1 (A_1) and D_n (A_n) are the left and right linkage sites of the donor (acceptor), respectively (as shown in Scheme 1). ϕ_{DA} denotes the torsional angle between the π-orbital of the donor and the acceptor unit. E and $\varepsilon_v^{\mathrm{A(D)}}$ correspond to the adiabatic energy in the triad oligomer and bridge orbitals, respectively. The summation runs over all molecular orbitals of the bridge. In the case of DTDPP-*n*T copolymers, which have an axial-symmetry system, $C^{\mathrm{dtdpp1}}_{\mathrm{HOMO(LUMO)}} = C^{\mathrm{dtdpp}n}_{\mathrm{HOMO(LUMO)}}$ and $\cos(\phi_{\mathrm{DA}}) = \cos(\phi_{\mathrm{AD}})$. The coefficient $C^{\mathrm{dtdpp1}(n\mathrm{T1})} C^{\mathrm{dtdpp}n(n\mathrm{Tn})}$ is equal to $\rho^{\mathrm{dtdpp1}(n\mathrm{T1})}_{\mathrm{(HOMO)LUMO}}$. Due to the good planarity of the systems, $\cos(\phi_{\mathrm{DA}}) = \cos(\phi_{\mathrm{AD}}) = 1$. With respect to the sandwich-type SE model, the main contribution of electron (hole) SE coupling comes from the interaction of the LUMO for DTDPP (HOMO for *n*T) with the LUMO (HOMO) of the bridge part, according to the decomposition of the SE coupling to the bridge orbital contribution (Table S1 in the ESI†). The adiabatic energy can be approximately regarded

as the polarized LUMO and HOMO energies of DTDDP for electrons and holes, respectively. Thus, eqn (7) can be simplified as:

$$V_{\mathrm{elec}}^{\mathrm{eff}} \propto \rho_{\mathrm{LUMO}}^{n\mathrm{T1}} \times \rho_{\mathrm{LUMO}}^{\mathrm{dtdpp1}} / (E_{\mathrm{LUMO}}^{\mathrm{dtdpp}} - E_{\mathrm{LUMO}}^{n\mathrm{T}}) \quad (8)$$

$$V_{\mathrm{hole}}^{\mathrm{eff}} \propto \rho_{\mathrm{HOMO}}^{n\mathrm{T1}} \times \rho_{\mathrm{HOMO}}^{\mathrm{dtdpp1}} / (E_{\mathrm{HOMO}}^{\mathrm{dtdpp}} - E_{\mathrm{HOMO}}^{n\mathrm{T}}) \quad (9)$$

Compared with eqn (8) and (9), the electron (hole) SE coupling is connected with the LUMO/HOMO molecular orbital density ($\rho_{\mathrm{LUMO}}^{n\mathrm{T1}} \times \rho_{\mathrm{LUMO}}^{\mathrm{dtdpp1}} / \rho_{\mathrm{HOMO}}^{n\mathrm{T1}} \times \rho_{\mathrm{HOMO}}^{\mathrm{dtdpp1}}$) at the linkage site and relative magnitude of the polarization energy difference ($(E_{\mathrm{LUMO}}^{\mathrm{dtdpp}} - E_{\mathrm{LUMO}}^{n\mathrm{T}})/(E_{\mathrm{HOMO}}^{\mathrm{dtdpp}} - E_{\mathrm{HOMO}}^{n\mathrm{T}})$). For different donor lengths, the HOMO and LUMO charge densities at linkage sites are close to each other for electrons and holes, as shown in Fig. 4(A), and thus, the charge transport polarity is determined by the latter term. The ratio of polarized $(E_{\mathrm{LUMO}}^{\mathrm{dtdpp}} - E_{\mathrm{LUMO}}^{n\mathrm{T}})/(E_{\mathrm{HOMO}}^{\mathrm{dtdpp}} - E_{\mathrm{HOMO}}^{n\mathrm{T}})$ is approximately the same as that of SE coupling for electrons and holes. The polarization effect has taken account into the site energy difference within the D–A copolymer environment. As can be seen from Fig. 3(A), after polarization, the HOMO and LUMO orbital energies simultaneously decrease for different lengths of thiophene. The polarization energy difference has a large difference compared to that of isolated systems. As can be seen from Fig. 4(B). The ratio of relative energy alignment $(E_{\mathrm{LUMO}}^{\mathrm{dtdpp}} - E_{\mathrm{LUMO}}^{n\mathrm{T}})/(E_{\mathrm{HOMO}}^{\mathrm{dtdpp}} - E_{\mathrm{HOMO}}^{n\mathrm{T}})$ for isolated DTDPP and nT moieties varies from 0.60 to 0.02, However, the ratio of polarized relative energy alignment $(E_{\mathrm{LUMO}}^{\mathrm{dtdpp}} - E_{\mathrm{LUMO}}^{n\mathrm{T}})/(E_{\mathrm{HOMO}}^{\mathrm{dtdpp}} - E_{\mathrm{HOMO}}^{n\mathrm{T}})$ changes from 1.6 to 0.9. The SE coupling depends on the polarized relative energy alignment, and the SE coupling for electrons changes from being larger than holes to close to each other for DTDPP-4T.

On the other hand, due to the charge density at the linkage atoms dropping significantly, the SE coupling for electrons presents a decreasing trend. Moreover, the charge density at the linkage sites decreased much faster than the energy difference, which induces the SE coupling to become smaller and smaller, since the longer the length, the weaker the charge distribution at the terminal atoms due to charge delocalization on the entire polymer chain. However, the hole SE coupling reveals an increasing trend from DTDPP-4T to DTDPP-5T, which is due to different SE models and different bridge orbital contributions, as listed in Table S1.†

From the above discussion, we found that the tendency of charge transport polarity change can be understood from intrachain SE coupling. For DTDPP-nT (n = 1, 3) the electron SE coupling is larger than the SE coupling for holes. For DTDPP-4T, since the relative energy alignment $(E_{\mathrm{LUMO}}^{\mathrm{dtdpp}} - E_{\mathrm{LUMO}}^{n\mathrm{T}})/(E_{\mathrm{HOMO}}^{\mathrm{dtdpp}} - E_{\mathrm{HOMO}}^{n\mathrm{T}})$ is close to 1, the balanced electron and hole superexchange transport is likely to take place. However, the hole SE coupling is larger than that of electrons for DTDPP-5T. Combined with the band edge shift, we can understand the charge transport polarity variation from experiments. Note that such polarity changes can also be understood from the perspective of chemical dilution. Namely, since the hole resides on the donor, as the donor length increases, it is natural that the hole transport becomes more and more dominant. Our SE model can give quantitative results.

3.3 The inter-chain charge transfer

Apart from intrachain process, inter chain charge transfer may happen and play an important role. So here, the inter-chain coupling of DTDPP-nT (n = 0–4) was also investigated. In Fig. 5(A), the theoretical model we used for studying inter-chain coupling, where the two oligomers are arranged in a face-to-face parallel configuration with a vertical distance fixed to be 3.6 Å (in experiments, it is generally 3.5 to 3.8 Å) and the short chain along long axis (Δx) and short axis (Δy). Based on the density functional method with the M062X functional,[57] which can give a good description of van der Waals weak interactions, we scan the binding energy and coupling for electrons and holes between oligomers in the molecular backbone plane.

Inter-chain coupling has a close connection with intermolecular stacking. Therefore, we scan the binding energy for different intermolecular stacking configurations. Comparing the binding energy of DTDDP, DTDPP-2t and DTDPP-4 (see Fig. S3 in the ESI†), we found that the lowest energy structures are located at points (4.5, 0), (6.5, 0) and (6.5, 0), corresponding to a shift of one thiophene unit along the long axis. As seen from Fig. S4,† the inter-chain stacking mode is with the donor facing the acceptor, determined by the electrostatic interaction. With the increase of donor length, the intermolecular stacking configuration does not alter such a D–A stacking trend. However, the increase of donor moiety length will change the

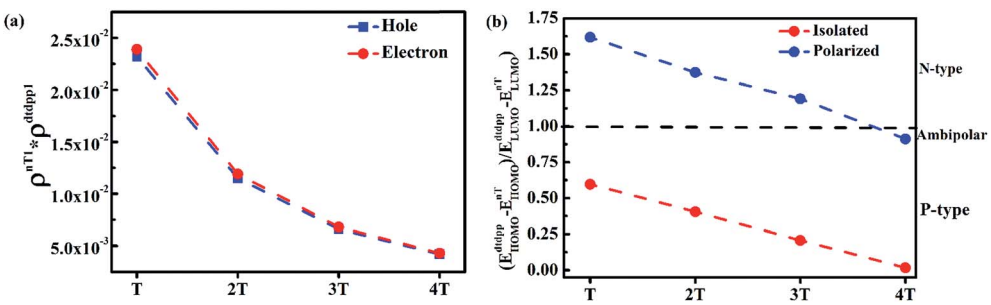

Fig. 4 (a) The charge density at the linkage atom for holes and electrons dependent on different thiophene lengths; (b) the ratio of energy difference for polarized and isolated moieties.

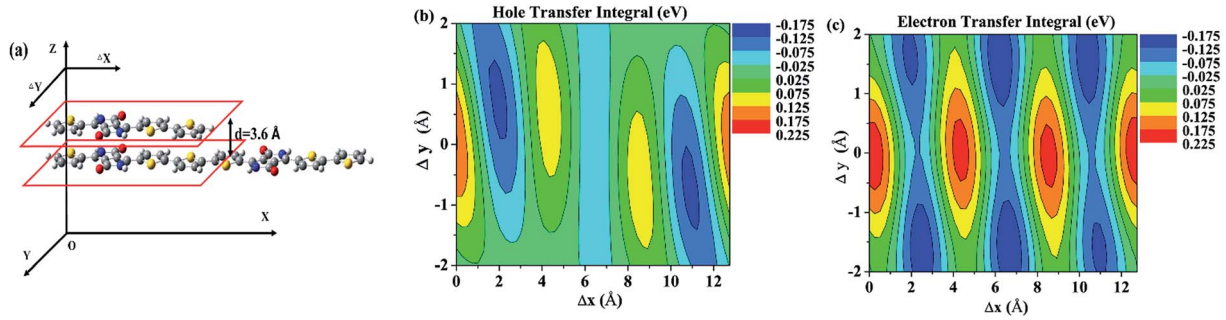

Fig. 5 (a) Calculation model for the inter-chain transfer integral; the inter-chain transfer integral for holes (b) and electrons (c) of DTDPP.

Table 1 The average value of the inter-chain transfer integral

System	t_h (meV)	t_e (meV)	t_h^2/t_e^2
DTDPP	50	85	0.35
DTDPP-T	53	90	0.35
DTDPP-2T	66	58	1.29
DTDPP-3T	63	48	1.72
DTDPP-4T	76	44	2.98

relative magnitude of intermolecular coupling for holes and electrons.

For DTDPP, the hole and the electron transfer integral has three oscillation periods, which depends on the nodal number of the HOMO/LUMO of DTDPP. The maximum points of the hole transfer integral are located at (0, 0), (2, 0.75), and (4.25, 1) and their corresponding centrosymmetric points and their corresponding transfer integral are 179, −139 and 107 meV, respectively. Considering that the energy at the points (0, 0) and (2, 0.75) is relatively high, there is a low possibility for locating at these two points, according to the Boltzmann distribution. Actually only the structure at (4.25, 1) whose transfer integral is 107 meV contributes primarily to hole transfer. For the electron transfer integral, the maximum points are located at (0, 0), (2.5, −1.5), (4.25, 0), and (6.5, −1.5) and their corresponding centrosymmetric points, and the values are 210, −160, 200, and −167 meV, respectively. The points at (0, 0), (2.5, −1.5), and (6.5, −1.5) are high energy points, so the most possible structure at the low energy point (4.25, 0) and a transfer integral of 107 meV should contribute primarily to electron transfer. It can be seen that for DTDPP, the inter-chain electron coupling is greater than the hole coupling. Although the maximum value of the electron transfer integral is higher than the highest value of the hole transfer integral, the electron and hole transfer integrals are close to each other when considering the binding energy distribution. Based on the Boltzmann distribution, taking the binding energy of the corresponding structure as the weighting factor, the mean value of the squared transfer integral is as follows:

$$\overline{t^2} = \frac{\sum_i t_i^2 \exp\left(-\frac{E_i - E_{\min}}{k_B T}\right)}{\sum_i \exp\left(-\frac{E_i - E_{\min}}{k_B T}\right)} \quad (10)$$

According to eqn (10), we can obtain the average value of the transfer integral, where i represents different stacking structures, t_i and E_i are the corresponding transfer integral and energy, and $E_{\min}$ is the global minimum energy. The average transfer integral of all systems is shown in Table 1. According to the Marcus formula, the hopping rate k is proportional to the square of the transfer integral. For DTDPP-nT, the ratio of the squares of hole and electron transfer integrals rises from 0.35 in DTDPP to 2.98 in DTDPP-4T. Therefore, inter-chain coupling also support the transport property change from n-type to ambipolar and then to p-type. It can be understood simply from the portion of donors, namely, hole hopping takes place at the HOMO of one donor to another *via* direct inter-chain coupling. A longer donor naturally contributes a larger inter-chain transfer integral.

4. Conclusions

Through first-principles computations, we found that there exist a continuous band gap and bandwidth variation for (DTDPP-nT) with the donor unit length increasing. Correspondingly, there exists a charge transport polarity transformation from n-type to ambipolar and finally to p-type. The band structure and charge transport polarity can be understood from the SE mechanism, band edge and inter-chain charge transport. For DTDPP-nT (n = 1, 3), electron SE coupling is larger than that of holes. Balanced electron and hole SE coupling is found for DNDPP-4T. In contrast, DTDPP-5T reveals p-type transport due to the staggered-type SE model. Based on the SE model, we shed light on the origin of the change transport polarity in view of the molecular level. Inter-chain coupling and the band edge contribute to a similar charge transport polarity change.

Conflicts of interest

There are no conflicts to declare.

Acknowledgements

This work is supported by the National Key R&D Program of China (2017YFA0204700), the National Natural Science Foundation of China (Grant Numbers: 21788102, 21673247,

21404067), the Strategic Priority Research Program of the Chinese Academy of Sciences (Grant No. XDB12020200) and Capacity Building for Sci-Tech Innovation-Fundamental Scientific Research Funds (025185305000). The computational work was carried out in the Tsinghua University High Performance Computing Centre.

References

1 G. Yu, J. Gao, J. C. Hummelen, F. Wudl and A. J. Heeger, *Science*, 1995, **270**, 1789.
2 S. Günes, H. Neugebauer and N. S. Sariciftci, *Chem. Rev.*, 2007, **107**, 1324–1338.
3 Y.-J. Cheng, S.-H. Yang and C.-S. Hsu, *Chem. Rev.*, 2009, **109**, 5868–5923.
4 M. Helgesen, R. Søndergaard and F. C. Krebs, *J. Mater. Chem.*, 2010, **20**, 36–60.
5 G. Li, R. Zhu and Y. Yang, *Nat. Photonics*, 2012, **6**, 153–161.
6 T. Ameri, N. Li and C. J. Brabec, *Energy Environ. Sci.*, 2013, **6**, 2390–2413.
7 X. Guo, R. P. Ortiz, Y. Zheng, Y. Hu, Y.-Y. Noh, K.-J. Baeg, A. Facchetti and T. J. Marks, *J. Am. Chem. Soc.*, 2011, **133**, 1405–1418.
8 C. Wang, H. Dong, W. Hu, Y. Liu and D. Zhu, *Chem. Rev.*, 2011, **112**, 2208–2267.
9 S. Holliday, J. E. Donaghey and I. McCulloch, *Chem. Mater.*, 2013, **26**, 647–663.
10 H. Li, F. S. Kim, G. Ren and S. A. Jenekhe, *J. Am. Chem. Soc.*, 2013, **135**, 14920–14923.
11 J. Mei, Y. Diao, A. L. Appleton, L. Fang and Z. Bao, *J. Am. Chem. Soc.*, 2013, **135**, 6724–6746.
12 Y. Zhao, Y. Guo and Y. Liu, *Adv. Mater.*, 2013, **25**, 5372–5391.
13 A. J. Heeger, *Chem. Soc. Rev.*, 2010, **39**, 2354–2371.
14 X. Zhang, H. Bronstein, A. J. Kronemeijer, J. Smith, Y. Kim, R. J. Kline, L. J. Richter, T. D. Anthopoulos, H. Sirringhaus and K. Song, *Nat. Commun.*, 2013, **4**, 2238.
15 G. Kim, S.-J. Kang, G. K. Dutta, Y.-K. Han, T. J. Shin, Y.-Y. Noh and C. Yang, *J. Am. Chem. Soc.*, 2014, **136**, 9477–9483.
16 D. Venkateshvaran, M. Nikolka, A. Sadhanala, V. Lemaur, M. Zelazny, M. Kepa, M. Hurhangee, A. J. Kronemeijer, V. Pecunia and I. Nasrallah, *Nature*, 2014, **515**, 384–388.
17 J. Yao, C. Yu, Z. Liu, H. Luo, Y. Yang, G. Zhang and D. Zhang, *J. Am. Chem. Soc.*, 2015, **138**, 173–185.
18 Z. Yi, X. Sun, Y. Zhao, Y. Guo, X. Chen, J. Qin, G. Yu and Y. Liu, *Chem. Mater.*, 2012, **24**, 4350–4356.
19 Z. Yi, L. Ma, B. Chen, D. Chen, X. Chen, J. Qin, X. Zhan, Y. Liu, W. J. Ong and J. Li, *Chem. Mater.*, 2013, **25**, 4290–4296.
20 T. Lei, J.-Y. Wang and J. Pei, *Acc. Chem. Res.*, 2014, **47**, 1117–1126.
21 C. Kanimozhi, N. Yaacobi-Gross, K. W. Chou, A. Amassian, T. D. Anthopoulos and S. Patil, *J. Am. Chem. Soc.*, 2012, **134**, 16532–16535.
22 A. Luzio, D. Fazzi, F. Nübling, R. Matsidik, A. Straub, H. Komber, E. Giussani, S. E. Watkins, M. Barbatti and W. Thiel, *Chem. Mater.*, 2014, **26**, 6233–6240.
23 R. Matsidik, H. Komber, A. Luzio, M. Caironi and M. Sommer, *J. Am. Chem. Soc.*, 2015, **137**, 6705–6711.
24 Y. Q. Zheng, T. Lei, J. H. Dou, X. Xia, J. Y. Wang, C. J. Liu and J. Pei, *Adv. Mater.*, 2016, **28**, 7213–7219.
25 J. Lee, A.-R. Han, H. Yu, T. J. Shin, C. Yang and J. H. Oh, *J. Am. Chem. Soc.*, 2013, **135**, 9540–9547.
26 M. Gruber, S.-H. Jung, S. Schott, D. Venkateshvaran, A. J. Kronemeijer, J. W. Andreasen, C. R. McNeill, W. W. Wong, M. Shahid and M. Heeney, *Chem. Sci.*, 2015, **6**, 6949–6960.
27 A. Han, G. K. Dutta, J. Lee, H. R. Lee, S. M. Lee, H. Ahn, T. J. Shin, J. H. Oh and C. Yang, *Adv. Funct. Mater.*, 2015, **25**, 247–254.
28 B. Sun, W. Hong, H. Aziz and Y. Li, *Polym. Chem.*, 2015, **6**, 938–945.
29 T. Lei, J.-Y. Wang and J. Pei, *Chem. Mater.*, 2013, **26**, 594–603.
30 Y. Yamashita, J. Tsurumi, F. Hinkel, Y. Okada, J. Soeda, W. Zajączkowski, M. Baumgarten, W. Pisula, H. Matsui and K. Müllen, *Adv. Mater.*, 2014, **26**, 8169–8173.
31 B. B. Y. Hsu, C. M. Cheng, C. Luo, S. N. Patel, C. Zhong, H. Sun, J. Sherman, B. H. Lee, L. Ying and M. Wang, *Adv. Mater.*, 2015, **27**, 7759–7765.
32 J. Lee, J. W. Chung, D. H. Kim, B.-L. Lee, J.-I. Park, S. Lee, R. Häusermann, B. Batlogg, S.-S. Lee and I. Choi, *J. Am. Chem. Soc.*, 2015, **137**, 7990–7993.
33 S. Schott, E. Gann, L. Thomsen, S. H. Jung, J. K. Lee, C. R. McNeill and H. Sirringhaus, *Adv. Mater.*, 2015, **27**, 7356–7364.
34 S. P. Senanayak, A. Ashar, C. Kanimozhi, S. Patil and K. Narayan, *Phys. Rev. B*, 2015, **91**, 115302.
35 J. Yang, Z. Zhao, H. Geng, C. Cheng, J. Chen, Y. Sun, L. Shi, Y. Yi, Z. Shuai and Y. Guo, *Adv. Mater.*, 2017, 29.
36 J. Van Vechten and T. Bergstresser, *Phys. Rev. B*, 1970, **1**, 3351.
37 R. Hill, *J. Phys. C: Solid State Phys.*, 1974, **7**, 521.
38 F. Capasso, *Science*, 1987, **235**, 172–177.
39 M. Schwarze, W. Tress, B. Beyer, F. Gao, R. Scholz, C. Poelking, K. Ortstein, A. A. Günther, D. Kasemann and D. Andrienko, *Science*, 2016, **352**, 1446–1449.
40 C. Murphy, M. Arkin, Y. Jenkins, N. Ghatlia, S. Bossmann, N. Turro and J. Barton, *Science*, 1993, **262**, 1025–1029.
41 H. Geng, X. Zheng, Z. Shuai, L. Zhu and Y. Yi, *Adv. Mater.*, 2015, **27**, 1443–1449.
42 H. Oberhofer, K. Reuter and J. Blumberger, *Chem. Rev.*, 2017, **117**, 10319–10357.
43 C. Cheng, H. Geng, Y. Yi and Z. Shuai, *J. Mater. Chem. C*, 2017, **5**, 3247.
44 W. Hong, B. Sun, H. Aziz, W.-T. Park, Y.-Y. Noh and Y. Li, *Chem. Commun.*, 2012, **48**, 8413–8415.
45 Z. Chen, M. J. Lee, R. Shahid Ashraf, Y. Gu, S. Albert-Seifried, M. Meedom Nielsen, B. Schroeder, T. D. Anthopoulos, M. Heeney and I. McCulloch, *Adv. Mater.*, 2012, **24**, 647–652.
46 J. D. Yuen, J. Fan, J. Seifter, B. Lim, R. Hufschmid, A. J. Heeger and F. Wudl, *J. Am. Chem. Soc.*, 2011, **133**, 20799–20807.

47 M. C. Gwinner, D. Kabra, M. Roberts, T. J. Brenner, B. H. Wallikewitz, C. R. McNeill, R. H. Friend and H. Sirringhaus, *Adv. Mater.*, 2012, **24**, 2728–2734.
48 J. Zaumseil, R. H. Friend and H. Sirringhaus, *Nat. Mater.*, 2006, **5**, 69–74.
49 C. Xiao, G. Zhao, A. Zhang, W. Jiang, R. A. Janssen, W. Li, W. Hu and Z. Wang, *Adv. Mater.*, 2015, **27**, 4963–4968.
50 Y. Li, P. Sonar, S. P. Singh, W. Zeng and M. S. Soh, *J. Mater. Chem.*, 2011, **21**, 10829–10835.
51 Z. Yi, S. Wang and Y. Liu, *Adv. Mater.*, 2015, **27**, 3589–3606.
52 B. N. Norris, S. Zhang, C. M. Campbell, *et al.*, *Macromolecules*, 2013, **46**, 1384–1392.
53 I. Y. Kanal, S. G. Owens, J. S. Bechtel and G. R. Hutchison, *J. Phys. Chem. Lett.*, 2013, **4**, 1613–1623.
54 B. SambathKumar, P. Shyam Vinod Kumar, F. S. Deepakrao, *et al.*, *J. Phys. Chem. C*, 2016, **120**, 26609–26619.
55 G. W. T. M. J. Frisch, H. B. Schlegel, G. E. Scuseria, M. A. Robb, J. R. Cheeseman, G. Scalmani, V. Barone, B. Mennucci, G. A. Petersson, H. Nakatsuji, M. Caricato, X. Li, H. P. Hratchian, A. F. Izmaylov, J. Bloino, G. Zheng, J. L. Sonnenberg, M. Hada, M. Ehara, K. Toyota, R. Fukuda, J. Hasegawa, M. Ishida, T. Nakajima, Y. Honda, O. Kitao, H. Nakai, T. Vreven, J. A. Montgomery Jr, J. E. Peralta, F. Ogliaro, M. Bearpark, J. J. Heyd, E. Brothers, K. N. Kudin, V. N. Staroverov, R. Kobayashi, J. Normand, K. Raghavachari, A. Rendell, J. C. Burant, S. S. Iyengar, J. Tomasi, M. Cossi, N. Rega, J. M. Millam, M. Klene, J. E. Knox, J. B. Cross, V. Bakken, C. Adamo, J. Jaramillo, R. Gomperts, R. E. Stratmann, O. Yazyev, A. J. Austin, R. Cammi, C. Pomelli, J. W. Ochterski, R. L. Martin, K. Morokuma, V. G. Zakrzewski, G. A. Voth, P. Salvador, J. J. Dannenberg, S. Dapprich, A. D. Daniels, Ö. Farkas, J. B. Foresman, J. V. Ortiz, J. Cioslowski and D. J. Fox, *Gaussian Inc.*, Wallingford CT, 2009.
56 R. Dovesi, R. Orlando, A. Erba, C. M. Zicovich-Wilson, B. Civalleri, S. Casassa, L. Maschio, M. Ferrabone, M. De La Pierre, P. D'Arco, Y. Noël, M. Causà, M. Rérat and B. Kirtman, *Int. J. Quantum Chem.*, 2014, **114**, 1287.
57 Y. Zhao and D. G. Truhlar, *Theor. Chem. Acc.*, 2008, **120**, 215–241.